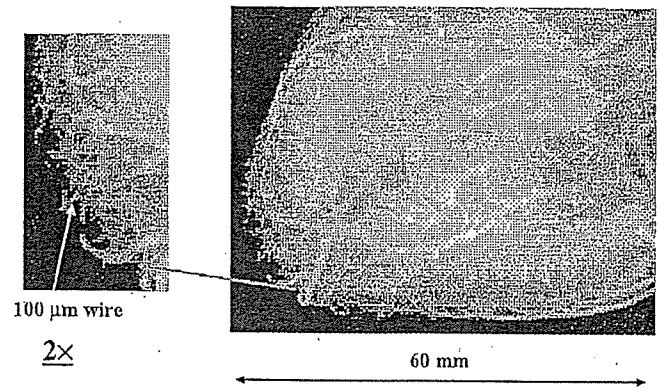

Fig. 10. Angiogram of an extracted dog heart using iodine microspheres.

5. DISCUSSION AND CONCLUSIONS

We employed an x-ray generator with a samarium-target tube and succeeded in producing samarium characteristic x-rays, which can be absorbed easily by iodine-based contrast media. Both the characteristic and bremsstrahlung x-ray intensities increased with increases in the tube voltage without filtering. Using the filter, K-rays were left by absorbing bremsstrahlung rays, and K-ray intensity increased with increases in the tube voltage.

Using this x-ray tube, we could produce K-series characteristic x-rays of nickel, copper, and molybdenum, and performed soft radiography. However it is difficult to produce clean samarium K-rays because bremsstrahlung x-ray intensity is in proportion to the atomic number. Therefore, optimum filters for absorbing bremsstrahlung rays should be employed to improve the image contrast of blood vessels.

Using the filter, the generator produced maximum number of characteristic photons was approximately 4×10^6 photons/($cm^2\cdot$ s) at 1.0 m from the source, and the photon count rate can be increased easily by improving the target. For example, the rotation anode tube can be developed, and sufficient x-ray dose rates could be produced by increasing the anode diameter.

ACKNOWLEDGMENT

This work was supported by Grants-in-Aid for Scientific Research (13470154, 13877114, and 16591222) and Advanced Medical Scientific Research from MECSST, Health and Labor Sciences Research Grants (RAMT-nano-001, RHGTEFB-genome-005 and RHGTEFB-saisei-003), and grants from the Keiryo Research Foundation, Promotion and Mutual Aid Corporation for Private Schools of Japan, Japan Science and Technology Agency (JST), and New Energy and Industrial Technology Development Organization (NEDO, Industrial Technology Research Grant Program in '03).

REFERENCES

1. H. Mori, K. Hyodo, E. Tanaka, M. U. Mohammed, A. Yamakawa, Y. Shinozaki, H. Nakazawa, Y. Tanaka, T. Sekka, Y. Iwata, S. Honda, K. Umetani, H. Ueki, T. Yokoyama, K. Tanioka, M. Kubota, H. Hosaka, N. Ishizawa and M. Ando, "Small-vessel radiography in situ with monochromatic synchrotoron radiation," *Radiology*, **201**, 173-177, 1996.

2. K. Hyodo, M. Ando, Y. Oku, S. Yamamoto, T. Takeda, Y. Itai, S. Ohtsuka, Y. Sugishita and J. Tada, "Development of a two-dimensional imaging system for clinical applications of intravenous coronary angiography using intense synchrotron radiation produced by a multipole wiggler," *J. Synchrotron Radiat.*, **5**, 1123-1126, 1998.

3. E. Sato, Y. Hayasi, R. Germer, E. Tanaka, H. Mori, T. Kawai, T. Ichimaru, K. Takayama and H. Ido, "Quasi-monochromatic flash x-ray generator utilizing weakly ionized linear copper plasma," *Rev. Sci. Instrum.*, **74**,

5236-5240, 2003.
4. E. Sato, Y. Hayasi, R. Germer, E. Tanaka, H. Mori, T. Kawai, T. Ichimaru, S. Sato, K. Takayama and H. Ido, "Sharp characteristic x-ray irradiation from weakly ionized linear plasma," *J. Electron Spectrosc. Related Phenom.*, **137-140**, 713-720, 2004.
5. E. Sato, E. Tanaka, H. Mori, T. Kawai, S. Sato and K. Takayama, "Clean monochromatic x-ray irradiation from weakly ionized linear copper plasma," *Opt. Eng.*, 44, 049002-1-6, 2005.
6. E. Sato, Y. Hayasi, R. Germer, E. Tanaka, H. Mori, T. Kawai, T. Inoue, A. Ogawa, S. Sato, K. Takayama, J. Onagawa, "X-ray spectra from weakly ionized linear copper plasma," *Jpn. J. Appl. Phys.*, **45**, 5301-5306, 2006.
7. E. Sato, E. Tanaka, H. Mori, T. Kawai, T. Inoue, A. Ogawa, S. Sato, K. Takayama and J. Onagawa, "Characteristic x-ray generator utilizing angle dependence of bremsstrahlung x-ray distribution," *Jpn. J. Appl. Phys.*, **45**, 2845-2849, 2006.
8. E. Sato, E. Tanaka, H. Mori, T. Kawai, T. Ichimaru, S. Sato, K. Takayama and H. Ido, "Demonstration of enhanced K-edge angiography using a cerium target x-ray generator," *Med. Phys,* **31**, 3017-3021, 2004.
9. E. Sato, A. Yamadera, E. Tanaka, H. Mori, T. Kawai, F. Ito, T. Inoue, A. Ogawa, S. Sato, K. Takayama, J. Onagawa and H. Ido, "X-ray spectra from a cerium target and their application to cone beam K-edge angiography," *Opt. Eng.*, 44, 096502-1-6, 2005.
10. E. Sato, E. Tanaka, H. Mori, T. Kawai, T. Inoue, A. Ogawa, A. Yamadera, S. Sato, F. Ito, K. Takayama, J. Onagawa and H. Ido, "Variations in cerium x-ray spectra and enhanced K-edge angiography," *Jpn. J. Appl. Phys.*, 44, 8204-8209, 2005.
11. E. Sato, K. Sato and Y. Tamakawa, "Film-less computed radiography system for high-speed imaging," *Ann. Rep. Iwate Med. Univ. Sch. Lib. Arts and Sci.*, **35**, 13-23, 2000.

*dresato@iwate-med.ac.jp; phone +81-19-651-5111; fax +81-19-654-9282

Japanese Journal of Applied Physics
Vol. 45, No. 4A, 2006, pp. 2845–2849

Characteristic X-ray Generator Utilizing Angle Dependence of Bremsstrahlung X-ray Distribution

Eiichi SATO, Etsuro TANAKA[1], Hidezo MORI[2], Toshiaki KAWAI[3], Takashi INOUE[4], Akira OGAWA[4], Shigehiro SATO[5], Kazuyoshi TAKAYAMA[6] and Jun ONAGAWA[7]

Department of Physics, Iwate Medical University, 3-16-1 Honchodori, Morioka 020-0015, Japan
[1]*Department of Nutritional Science, Faculty of Applied Bio-science, Tokyo University of Agriculture, 1-1-1 Sakuragaoka, Setagaya-ku, Tokyo 156-8502, Japan*
[2]*Department of Cardiac Physiology, National Cardiovascular Center Research Institute, 5-7-1 Fujishirodai, Suita, Osaka 565-8565, Japan*
[3]*Electron Tube Division #2, Hamamatsu Photonics K.K., 314-5 Shimokanzo, Iwata, Shizuoka 438-0193, Japan*
[4]*Department of Neurosurgery, School of Medicine, Iwate Medical University, 19-1 Uchimaru, Morioka 020-8505, Japan*
[5]*Department of Microbiology, School of Medicine, Iwate Medical University, 19-1 Uchimaru, Morioka 020-8505, Japan*
[6]*Shock Wave Research Center, Institute of Fluid Science, Tohoku University, 2-1-1 Katahira, Sendai 980-8577, Japan*
[7]*Department of Applied Physics and Informatics, Faculty of Engineering, Tohoku Gakuin University, 1-13-1 Chuo, Tagajo, Miyagi 985-8537, Japan*

(Received November 17, 2005; revised December 24, 2005; accepted December 31, 2005; published online April 7, 2006)

This generator consists of the following components: a constant high-voltage power supply, a filament power supply, a turbomolecular pump, and an X-ray tube. The X-ray tube is a demountable diode which is connected to the turbomolecular pump and consists of the following major devices: a molybdenum rod target, a tungsten hairpin cathode (filament), a focusing (Wehnelt) electrode, a polyethylene terephthalate X-ray window 0.25 mm in thickness, and a stainless-steel tube body. In the X-ray tube, the positive high voltage is applied to the anode (target) electrode, and the cathode is connected to the tube body (ground potential). In this experiment, the tube voltage applied was from 22 to 36 kV, and the tube current was regulated to within 100 μA by the filament temperature. The exposure time is controlled in order to obtain optimum X-ray intensity. The electron beams from the cathode are converged to the target by the focusing electrode, and clean K-series characteristic X-rays are produced through the focusing electrode without using a filter. The X-ray intensity was 26.6 μGy/s at 1.0 m from the X-ray source with a tube voltage of 30 kV and a tube current of 100 μA, and quasi-monochromatic radiography was performed using a computed radiography system. [DOI: 10.1143/JJAP.45.2845]

KEYWORDS: demountable X-ray tube, electron-impact source, quasi-monochromatic X-rays, K-series characteristic X-rays, Sommerfeld's theory

1. Introduction

A great deal of effort has been devoted to the research and development of X-ray lasers in past years, and several different generators have been developed. Using tera-watt pulse lasers as pumping sources, a transient collisional excitation method has been proposed.[1)] Subsequently, capillary discharge soft X-ray laser generators[2–4)] have been developed and demonstrated. However, it is difficult to produce high-photon-energy X-ray lasers with energies 10 keV or beyond.

Recently, we have developed several different flash X-ray generators[5–9)] corresponding to specific radiographic objectives, and the plasma X-ray source has been growing with increases in the electrostatic energy in the condenser. By forming weakly ionized linear plasma using rod targets, we confirmed irradiation of clean K-series characteristic X-rays such as hard X-ray lasers from the plasma axial direction using a table-top flash X-ray generator.[10–13)] This super fluorescence has been employed to perform cone-beam monochromatic radiography such as iodine K-edge and gadolinium K-edge angiographies. Furthermore, because higher harmonic hard X-rays have been produced from the copper plasma, we have to confirm the irradiations of higher harmonics with charges in the target element.

Without forming plasmas, demountable flash X-ray tubes can be employed to perform fundamental study on producing monochromatic X-rays,[14)] and have succeeded in producing clean K-series characteristic X-rays. However, monochromatic flash radiography has had difficulties in controlling X-ray duration, and in performing magnification radiography including phase-contrast effect.

At present, brilliant monochromatic parallel X-ray beams from synchrotron radiation are used in various fields including medical imaging,[15–17)] and large-scale X-ray free electron laser sources[18)] are constructing as a new-generation radiation source for producing monochromatic coherent X-rays. In contrast, small-scale steady-state monochromatic parallel and cone beams can be employed to perform medical imaging including phase-contrast radiography and K-edge angiography[19)] in hospitals.

In this paper, we developed an X-ray generator used to perform a preliminary experiment for generating clean K-series characteristic X-rays by angle dependence of the bremsstrahlung X-rays.

2. Generator

Figure 1 shows a block diagram of a compact characteristic (quasi-monochromatic) X-ray generator. This generator consists of the following components: a constant high-voltage power supply (SL150, Spellman), a DC filament power supply, a turbomolecular pump, and an X-ray tube. The structure of the X-ray tube is illustrated in Fig. 2. The X-ray tube is a demountable diode which is connected to the turbomolecular pump with a pressure of approximately 0.5 mPa and consists of the following major devices: a molybdenum rod target of 3.0 mm in diameter, a tungsten hairpin cathode (filament), a focusing (Wehnelt) electrode, a polyethylene terephthalate X-ray window 0.25 mm in thickness, and a stainless-steel tube body. In the X-ray tube, the positive high voltage is applied to the anode (target) electrode, and the cathode is connected to the tube body

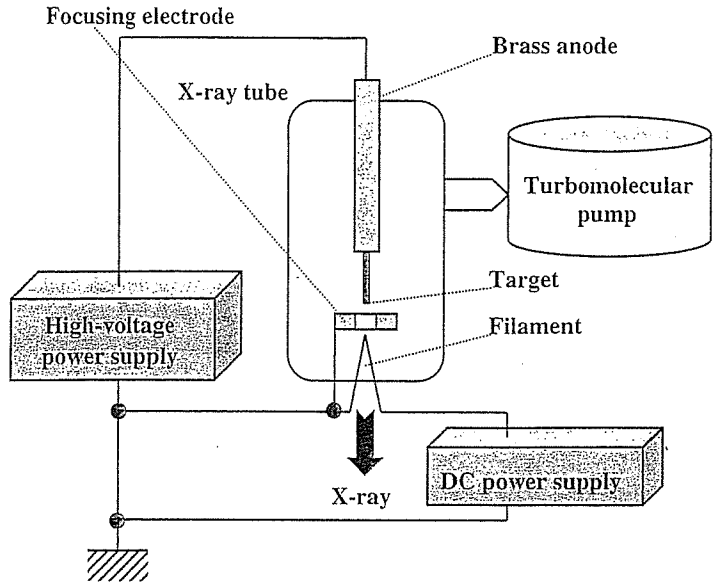

Fig. 1. Block diagram including the main transmission line of the compact X-ray generator with a quasi-monochromatic diode.

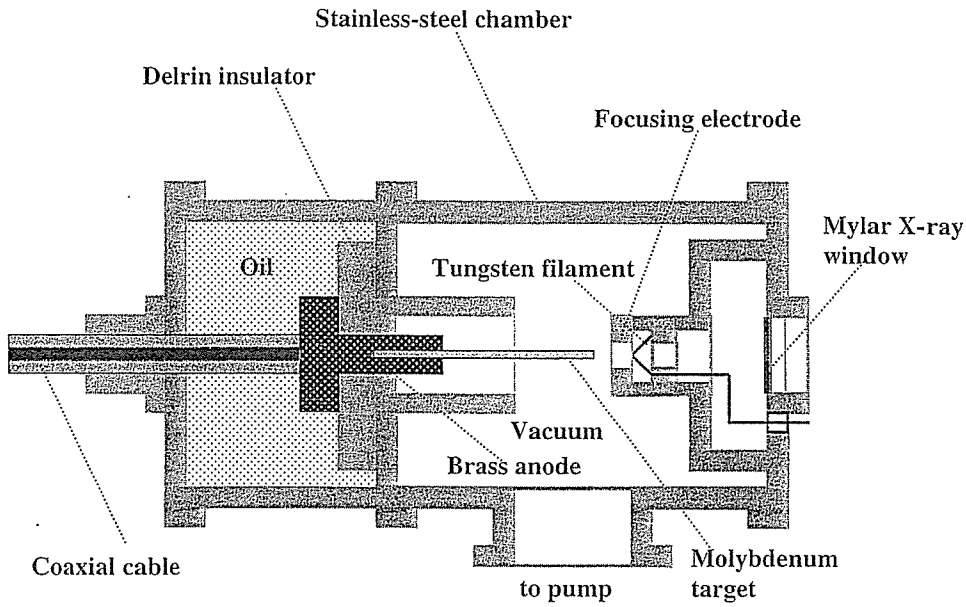

Fig. 2. Schematic drawing of the quasi-monochromatic X-ray tube.

(ground potential). In this experiment, the tube voltage applied was from 22 to 36 kV, and the tube current was regulated to within 100 μA by the filament temperature. The exposure time is controlled in order to obtain optimum X-ray intensity. The electron beams from the cathode are converged to the target by the focusing electrode, and X-rays are produced through the focusing electrode. Because bremsstrahlung rays are not emitted in the opposite direction to that of electron trajectory in Sommerfeld's theory[20] (Fig. 3), clean molybdenum K-series X-rays can be produced without using a filter.

3. Characteristics

3.1 X-ray intensity

X-ray intensity was measured by a Victoreen 660 ionization chamber at 1.0 m from the X-ray source (Fig. 4). At a constant tube current of 100 μA, the X-ray intensity increased when the tube voltage was increased. In this measurement, the intensity with a tube voltage of 30 kV and a current of 0.10 mA was 26.6 μGy/s at 1.0 m from the source.

3.2 X-ray source

In order to measure images of the X-ray source, we employed a pinhole camera with a hole diameter of 100 μm in conjunction with a computed radiography (CR) system[21] (Fig. 5). When the tube voltage was increased, the spot diameter slightly increased and had a maximum value of approximately 2.5 mm.

3.3 X-ray spectra

X-ray spectra were measured using a transmission-type spectrometer with a lithium fluoride curved crystal 0.5 mm in thickness. The X-ray intensities of the spectra were

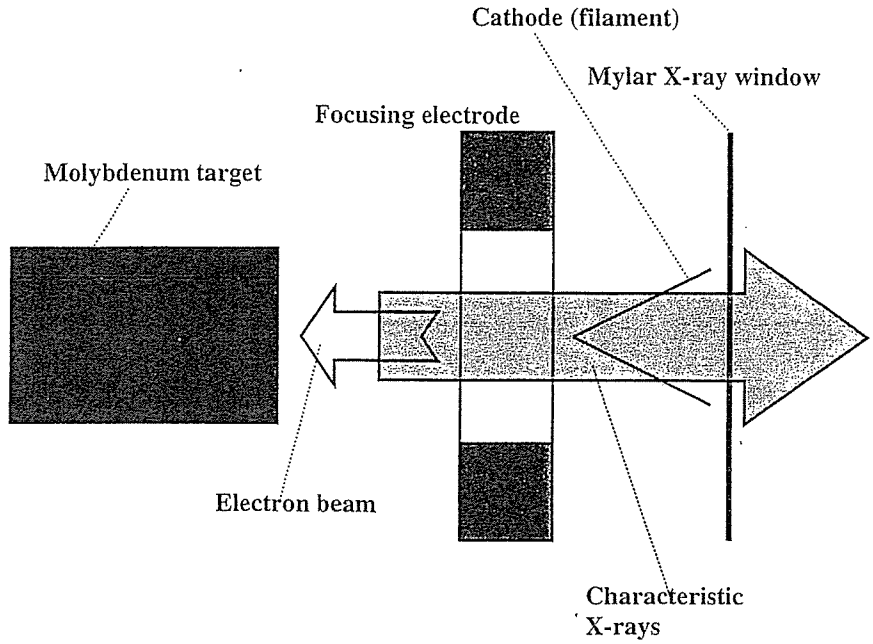

Fig. 3. K-photon irradiation from the X-ray tube.

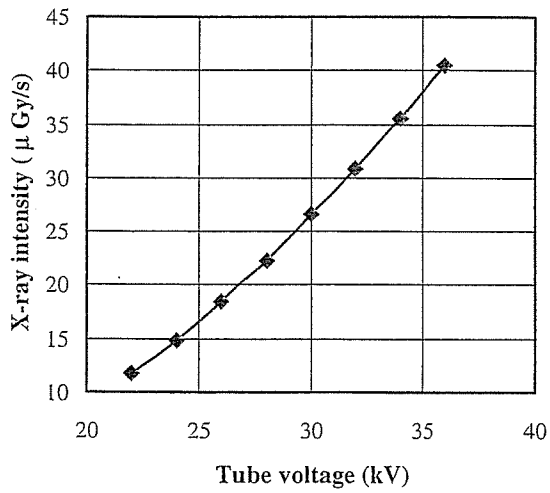

Fig. 4. X-ray intensity at 1.0 m from the X-ray source according to changes in the tube voltage with a tube current of 100 μA.

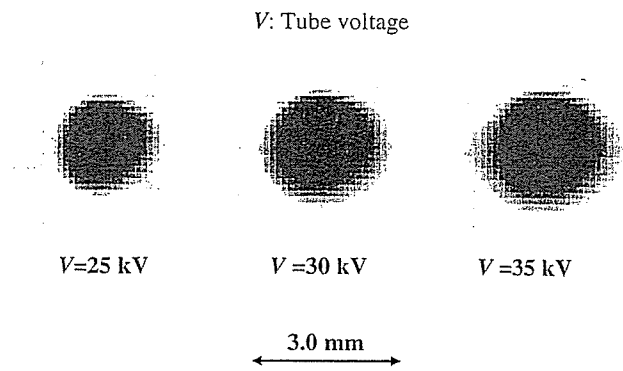

Fig. 5. Images of the characteristic X-ray source obtained using a pinhole camera with changes in the tube voltage.

detected by an imaging plate of the CR system (Konica Minolta, Regius 150) with a wide dynamic range, and relative X-ray intensity was calculated from Dicom original digital data corresponding to X-ray intensity; the data was scanned by Dicom viewer in the film-less CR system. Subsequently, the relative X-ray intensity as a function of the data was calibrated using a conventional X-ray generator, and we confirmed that the intensity was proportional to the exposure time. Figure 6 shows measured spectra from the molybdenum target. We observed clean K lines, while bremsstrahlung rays were hardly detected. The characteristic X-ray intensity substantially increased with increases in the tube voltage.

4. Radiography

The quasi-monochromatic radiography was performed by the CR system at 1.0 m from the X-ray source with the filter, and the tube voltage was 30 kV.

Firstly, rough measurements of image resolution were made using wires. Figure 7 shows radiograms of tungsten wires coiled around pipes made of poly(methyl methacrylate) (PMMA). Although the image contrast increased with increases in the wire diameter, a 50 μm-diameter wire could be observed.

A radiogram of a vertebra is shown in Fig. 8, and the fine structure of the vertebra was observed. Next, angiography was performed using iodine microspheres of 15 μm in diameter. Figures 9 and 10 show angiograms of a rabbit heart and thigh, respectively, and we could obtained high contrast images of coronary arteries and fine blood vessels.

5. Conclusions and Outlook

In summary, we developed a new quasi-monochromatic X-ray generator with a molybdenum-target tube and succeeded in producing clean molybdenum K lines. The characteristic X-ray intensity increased with increases in the tube voltage, and monochromatic Kα rays were left by a zirconium filter.

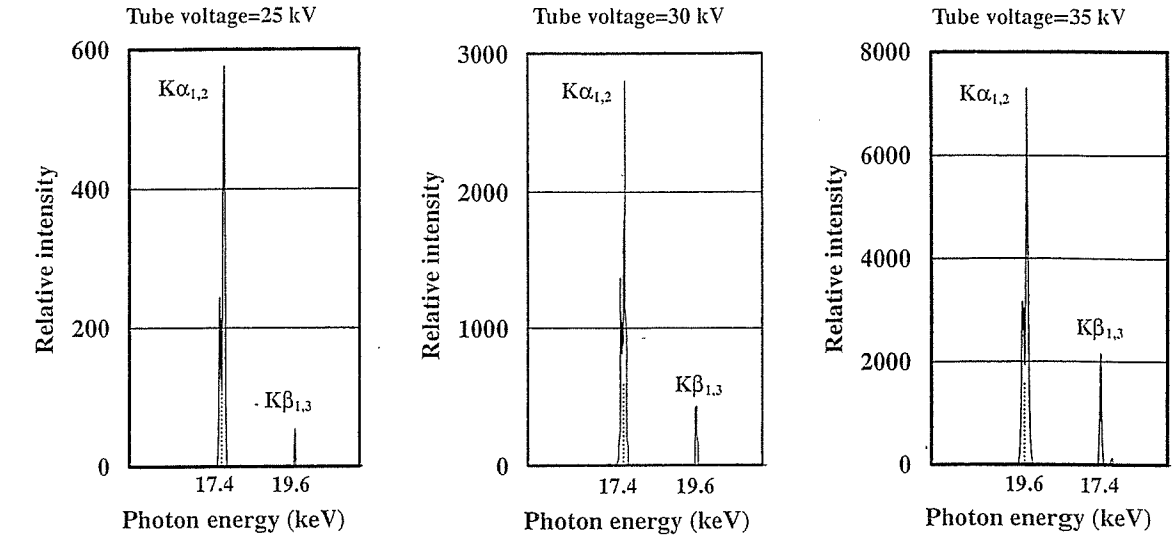

(a)

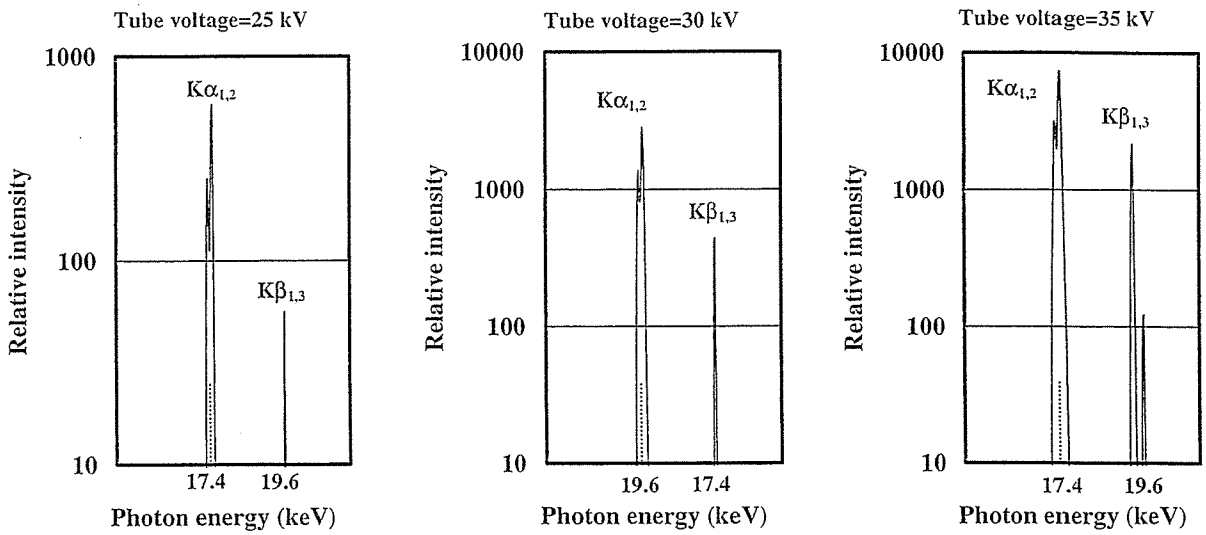

(b)

Fig. 6. X-ray spectra from the molybdenum target with (a) an ordinate scale and (b) a logarithmic scale. The spectra were measured using a transmission type spectrometer with a lithium fluoride curved crystal.

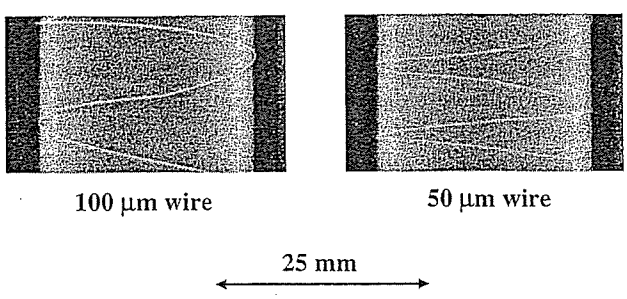

Fig. 7. Radiograms of tungsten wires of 50 and 100 μm in diameter coiled around pipes made of polymethyl methacrylate.

In this preliminary experiment, although the maximum tube voltage and current were 36 kV and 0.10 mA, the voltage and current could be increased to 100 kV and 1.0 mA, respectively. Under the pulsed operation, the current can be increased to approximately 1 A without considering

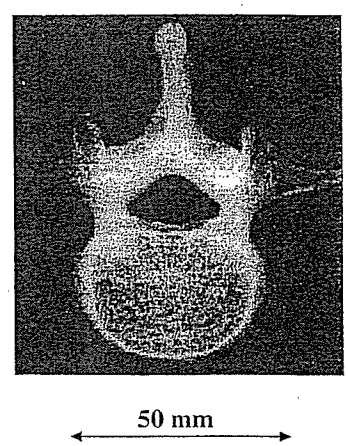

Fig. 8. Radiogram of a vertebra. Fine structure of the vertebra were visible.

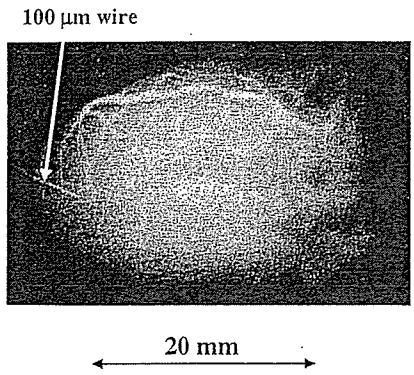

Fig. 9. Angiograms of a rabbit heart. Coronary arteries were visible.

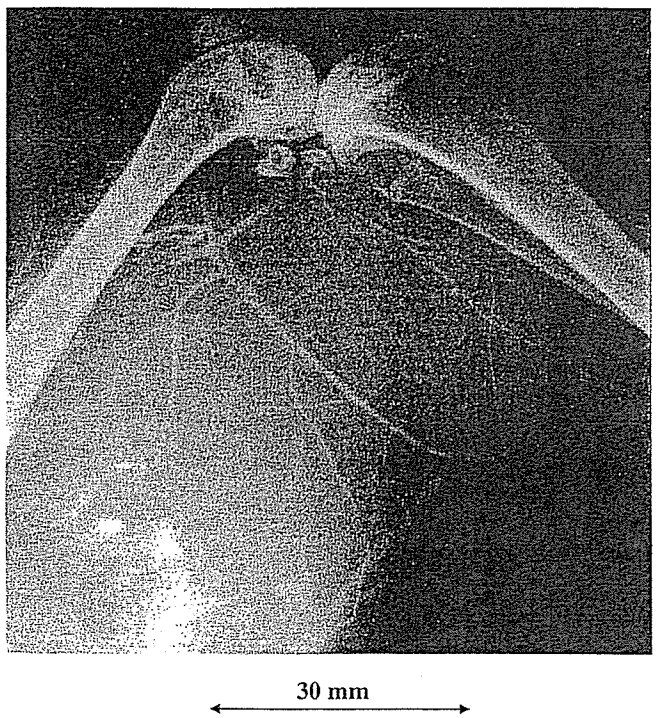

Fig. 10. Angiogram of a rabbit thigh. Fine blood vessels of approximately 100 μm were visible.

the target evaporation. Subsequently, the generator produced maximum number of characteristic photons was approximately 1×10^8 photons/(cm^2·s) at 1.0 m from the source, and the photon count rate can be increased easily by increasing the current.

In the present research, the molybdenum K-series characteristic X-rays are useful for mammography, and the photon energies of characteristic X-rays can be selected by the target element. In particular, enhanced K-edge angiography can be performed using a cerium target because cerium Kα rays (34.6 keV) are absorbed easily by iodine-based contrast media with an iodine K-edge of 33.2 keV. Using this angiography, coronary arteries and fine blood vessels formed in regenerative medicine may be observed with high contrasts. Furthermore, a flat panel detector is useful to observe blood flows for cases of cardiovascular disease.

Acknowledgment

This work was supported by Grants-in-Aid for Scientific Research (13470154, 13877114, and 16591222) and Advanced Medical Scientific Research from MECSST, Grants from Keiryo Research Foundation, The Promotion and Mutual Aid Corporation for Private School of Japan, JST (Test of Fostering Potential), NEDO, and MHLW (HLSRG, RAMT-nano-001, RHGTEFB-genome-005, and RGCD13C-1).

1) K. Nagashima, M. Tanaka, M. Nishikino, M. Kishimoto, M. Kado, T. Kawachi, N. Hasegawa, Y. Ochi, K. Sukegawa, R. Tai and K. Kato: Proc. SPIE **5197** (2003) 1.
2) J. J. Rocca, V. Shlyaptsev, F. G. Tomasel, O. D. Cortazar, D. Hartshorn and J. L. A. Chilla: Phys. Rev. Lett. **73** (1994) 2192.
3) C. D. Macchietto, B. R. Benware and J. J. Rocca: Opt. Lett. **24** (1999) 1115.
4) J. J. G. Rocca, J. L. A. Chilla, S. Sakadzic, A. Rahman, J. Filevich, E. Jankowska, E. C. Hammarsten, B. M. Luther, H. C. Kapteyn, M. Murnane and V. N. Shlyapsev: Proc. SPIE **4505** (2001) 1.
5) E. Sato, S. Kimura, S. Kawasaki, H. Isobe, K. Takahashi, Y. Tamakawa and T. Yanagisawa: Rev. Sci. Instrum. **61** (1990) 2343.
6) K. Takahashi, E. Sato, M. Sagae, T. Oizumi, Y. Tamakawa and T. Yanagisawa: Jpn. J. Appl. Phys. **33** (1994) 4146.
7) E. Sato, K. Takahashi, M. Sagae, S. Kimura, T. Oizumi, Y. Hayasi, Y. Tamakawa and T. Yanagisawa: Med. Biol. Eng. Comput. **32** (1994) 289.
8) E. Sato, M. Sagae, K. Takahashi, A. Shikoda, T. Oizumi, Y. Hayasi, Y. Tamakawa and T. Yanagisawa: Med. Biol. Eng. Comput. **32** (1994) 295.
9) E. Sato, E. Tanaka, H. Mori, T. Kawai, T. Ichimaru, S. Sato, K. Takayama and H. Ido: Med. Phys. **32** (2005) 49.
10) E. Sato, Y. Hayasi, R. Germer, E. Tanaka, H. Mori, T. Kawai, T. Ichimaru, K. Takayama and H. Ido: Rev. Sci. Instrum. **74** (2003) 5236.
11) E. Sato, Y. Hayasi, R. Germer, E. Tanaka, H. Mori, T. Kawai, T. Ichimaru, S. Sato, K. Takayama and H. Ido: J. Electron Spectrosc. Relat. Phenom. C **137–140** (2004) 713.
12) E. Sato, E. Tanaka, H. Mori, T. Kawai, S. Sato and K. Takayama: Opt. Eng. **44** (2005) 049002.
13) E. Sato, R. Germer, E. Tanaka, H. Mori, T. Kawai, T. Ichimaru, S. Sato, H. Ojima, K. Takayama and H. Ido: Proc. SPIE **5580** (2005) 146.
14) E. Sato, M. Sagae, E. Tanaka, Y. Hayasi, R. Germer, H. Mori, T. Kawai, T. Ichimaru, S. Sato, K. Takayama and H. Ido: Jpn. J. Appl. Phys. **43** (2004) 7324.
15) A. Momose, T. Takeda, Y. Itai and K. Hirano: Nat. Med. **2** (1996) 473.
16) H. Mori *et al.*: Radiology **201** (1996) 173.
17) K. Hyodo, M. Ando, Y. Oku, S. Yamamoto, T. Takeda, Y. Itai, S. Ohtsuka, Y. Sugishita and J. Tada: J. Synchrotron Radiat. **5** (1998) 1123.
18) K. Lan, E. E. Fill and J. M. Vehn: Proc. SPIE **5197** (2003) 253.
19) E. Sato, E. Tanaka, H. Mori, T. Kawai, T. Ichimaru, S. Sato, K. Takayama and H. Ido: Med. Phys. **31** (2004) 3017.
20) B. K. Agarwal: *X-ray Spectroscopy* (Springer-Verlag, New York, 1991) 2nd ed., p. 18.
21) E. Sato, K. Sato and Y. Tamakawa: Annu. Rep. Iwate Med. Univ. School Lib. Arts Sci. **35** (2000) 13.

Cardiovasc Drugs Ther (2006) 20: 159–165
DOI 10.1007/s10557-006-8285-8

BASIC RESEARCH

Granulocyte Colony-Stimulating Factor Mediates Cardioprotection Against Ischemia/Reperfusion Injury via Phosphatidylinositol-3-Kinase/Akt Pathway in Canine Hearts

Hiroyuki Takahama · Tetsuo Minamino · Akio Hirata · Akiko Ogai · Hiroshi Asanuma · Masashi Fujita · Masakatsu Wakeno · Osamu Tsukamoto · Ken-ichiro Okada · Kazuo Komamura · Seiji Takashima · Yoshiro Shinozaki · Hidezo Mori · Naoki Mochizuki · Masafumi Kitakaze

Published online: 16 June 2006

Abstract
Purpose Recent studies suggest that G-CSF prevents cardiac remodeling following myocardial infarction (MI) likely through regeneration of the myocardium and coronary vessels. However, it remains unclear whether G-CSF administered at the onset of reperfusion prevents ischemia/reperfusion injury in the acute phase. We investigated acute effects of G-CSF on myocardial infarct size and the incidence of lethal arrhythmia and evaluated the involvement of the phosphatidylinositol-3 kinase (PI3K) in the *in vivo* canine models.
Methods In open-chest dogs, left anterior descending coronary artery (LAD) was occluded for 90 minutes followed by 6 hours of reperfusion. We intravenously administered G-CSF (0.33 μ/kg/min) for 30 minutes from the onset of reperfusion. Wortmannin, a PI3K inhibitor, was selectively administered into the LAD after the onset of reperfusion.
Results G-CSF significantly ($p < 0.05$) reduced myocardial infarct size (38.7±4.3% to 15.7±5.3%) and the incidence of ventricular fibrillation during reperfusion periods (50% to 0%) compared with the control. G-CSF enhanced Akt phospholylation in ischemic canine myocardium. Wortmannin blunted both the infarct size-limiting and anti-arrhythmic effects of G-CSF. G-CSF did not change myeloperoxidase activity, a marker of neutrophil accumulation, in the infarcted myocardium.
Conclusion An intravenous administration of G-CSF at the onset of reperfusion attenuates ischemia/reperfusion injury through PI3K/Akt pathway in the *in vivo* model. G-CSF administration can be a promising candidate for the adjunctive therapy for patients with acute myocardial infarction.

Takahama and Hirata contributed equally to this work.

H. Takahama · A. Ogai · H. Asanuma · M. Wakeno · K. Komamura · H. Mori · M. Kitakaze
Department of Cardiovascular Medicine,
National Cardiovascular Center,
Suita 565-8565, Osaka, Japan

H. Takahama · M. Wakeno · N. Mochizuki
Department of Structural Analysis,
National Cardiovascular Center,
Suita 565-8565, Osaka, Japan

H. Takahama · M. Wakeno · N. Mochizuki
Department of Bioregulatory Medicine,
Osaka University Graduate School of Medicine,
Suita 565-0871, Osaka, Japan

T. Minamino (✉) · A. Hirata · M. Fujita · O. Tsukamoto · K.-i. Okada · S. Takashima
Department of Cardiovascular Medicine,
Osaka University Graduate School of Medicine,
2-2 Yamadaoka, Suita 565-0871, Osaka, Japan
e-mail: minamino@medone.med.osaka-u.ac.jp

Y. Shinozaki
Department of Physiological Science,
Tokai University School of Medicine,
Isehara 259-1193, Kanagawa, Japan

Key words G-CSF · myocardial infarction · ischemia-reperfusion injury · ventricular fibrillation · phosphatidylinositol-3 kinase · Akt

Abbreviations

VF	ventricular fibrillation.
G-CSF	granulocyte colony-stimulating factor
WTMN	wortmannin

Introduction

Granulocyte colony-stimulating factor (G-CSF), a 20-kDa glycoprotein, promotes the proliferation, survival and differentiation of hematopoietic cells [1]. Furthermore, G-CSF can mobilize hematopoietic stem cells from bone marrow [2, 3]. Thus, G-CSF is believed to improve cardiac remodeling after myocardial infarction (MI) through regeneration of the myocardium and angiogenesis [4, 5]. In addition to these effects of G-CSF, Komuro and colleagues clearly demonstrated that the high dose of G-CSF acutely reduces infarct size by preventing apoptosis in the isolated hearts [6]. However, it remains unclear whether clinically relevant dosages of G-CSF can reduce the infarct size in the in vivo model and, if so, it is not clear which downstream signaling pathway is involved in the acute cardioprotective effects of G-CSF. Furthermore, although lethal arrhythmias are a major cause of death in patients with acute myocardial infarction [7, 8], anti-arrhythmic effects of G-CSF have not been determined.

Thus, we investigated the acute effects of a clinical relevant dose of G-CSF on ischemia/reperfusion injury including both lethal arrhythmias and infarct size in canine hearts. We also examined a role of the PI3K/Akt pathway, a down stream of G-CSF receptors, in the cardioprotective effects of G-CSF. In the present study, we adopted ischemia/reperfusion protocols that have not been tested in previous studies [4, 5], because coronary revascularization has been established as a standard therapy to attenuate cardiac damage after MI.

Materials and methods

Materials

G-CSF was provided by Kirin brewery company (Tokyo, Japan). Recombinant human G-CSF can increase the number of white blood cells in dogs [9]. Wortmannin was obtained from Sigma (St. Louis, MO), and antibodies against Phospho-Akt and Akt were obtained from Cell signaling technologies (Beverly, MA).

Instrumentation

Twenty-nine beagle dogs (Kitayama Labes, Gifu, Japan) weighing 8 to 12 kg were anesthetized by an intravenous injection of sodium pentobarbital (30 mg/kg), intubated and ventilated with room air mixed with oxygen (100% O_2 at flow rate of 1.0 to 1.5 l/min). Thoracotomy was done at the fifth left intercostal space, and the heart was suspended in a pericardial cradle. After intravenous administration of heparin (500 U/kg), the left anterior descending coronary artery (LAD) was cannulated for perfusion with blood from the left carotid artery through an extracorporeal bypass tube. This allows the selective infusion of drugs into the LAD-perfused areas through this bypass tube. The left atrium was catheterized for microsphere injection to measure myocardial collateral blood flow during ischemia as described previously [10]. Hydration was maintained by a slow normal saline infusion. Both systemic blood pressure (SBP) and heart rate (HR) were monitored continuously during the study. All procedures were performed in conformity with the Guide for the care and use of laboratory animals (NIH Publication No. 85–23, 1996 revision), and were approved by the *Osaka University Committee for Laboratory Animal Use.*

Experimental protocols

Protocol 1. Acute effects of G-CSF on infarct size and lethal arrhythmias in canine hearts

After hemodynamic stabilization, we intravenously administered either saline (Control group; $n = 9$) or G-CSF (0.33 μg/kg/min) (G-CSF group; $n = 6$) for 30 min following the onset of reperfusion. An intracoronary administration of wortmannin (WTMN), a PI3K inhibitor, was selectively administered into the LAD (1.5 μg/kg/min) for 60 min after the onset of reperfusion (GCSF + WTMN group, $n = 7$; WTMN group, $n = 7$) (Fig. 1). We have previously confirmed that the dose of wortmannin used prevents the phosphorylation of Akt in myocardium [10]. We measured infarct size and myocardial collateral blood flow during ischemia. In brief, infarct size was evaluated at the end of the protocol by Evans blue/TTC staining. Collateral blood flow during 90 min of ischemia was assessed by the non-radioactive microsphere method [10]. We also counted

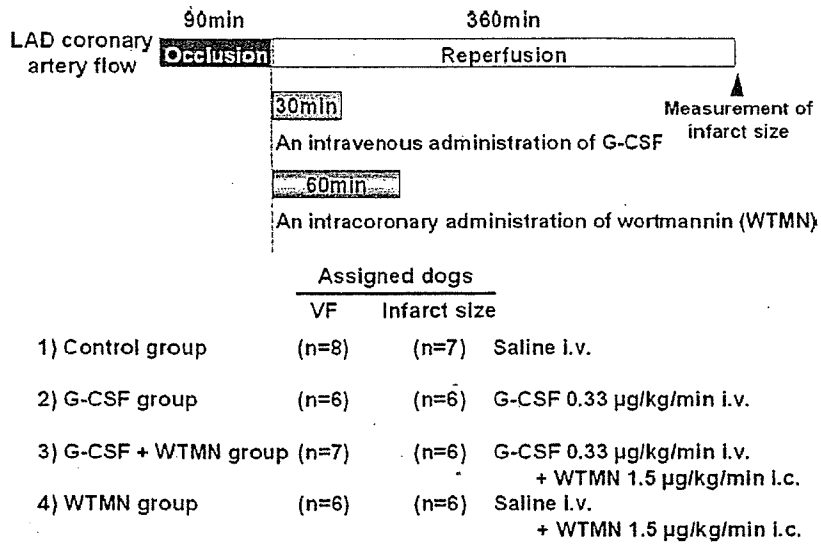

Fig. 1 Experimental protocols to assess myocardial infarct size and ventricular fibrillation (VF) in canine hearts. Myocardial infarct size was measured after 90 min of left anterior descending coronary artery (LAD) occlusion followed by 360 min of reperfusion. The incidence of VF was evaluated during reperfusion for 360 min. Intravenous administration of granulocyte colony-stimulating factor (G-CSF) was started at the onset of reperfusion and continued for 30 min. Intracoronary administration of wortmannin (WTMN) was started at the onset of reperfusion and continued for 60 min.

the incidence of VF during the 6 h reperfusion period (Fig. 1).

Finally, we measured myeloperoxidase (MPO) activity in LAD-perfused myocardium to check the accumulation of neutrophils in infarcted myocardium.

Protocol 2. Phosphorylation of Akt in ischemic myocardium

In this protocol, we used 11 dogs in Control group ($n = 3$), G-CSF group ($n = 4$), and G-CSF + WTMN group ($n = 4$). After 90 min of ischemia followed by 30 min of reperfusion, hearts were excised. The myocardial tissue in the ischemic zone, which was identified as the edge of the region showing necrosis, and non-ischemic zone were quickly placed into liquid nitrogen and stored at −80°C. Phosphorylation of Akt and total content of Akt were evaluated by immunoblotting as reported previously [10].

Immunoblotting

Immunoblotting was performed as described previously [11], and the immunoreactive bands were quantified by densitometry (Molecular Dynamics).

MPO activity

Several myocardial tissue samples were taken from the ischemic area in the dogs studied, frozen in liquid nitrogen and stored at −80°C until assay. The technical procedure has been described previously [12]. One unit of MPO activity was defined as that which degrades 1 μmol hydrogen peroxide per minute at 25°C.

Statistical analysis

Results are expressed as the mean ± SEM. Comparisons of the time course of the change in mean SBP and HR between groups were performed using two-way repeated measures analysis of variance (ANOVA). Comparisons of other data between groups were performed using one-way factional ANOVA. The Bonferroni-Holm procedure was used for correction of multiple comparisons [13]. The incidence of VF was compared using the χ^2-test and Fisher's exact probability test. A p value < 0.05 was considered to represent statistical significance.

Results

Criteria for exclusion

Since there was a negative correlation between myocardial collateral blood flow during ischemia and the incidence of VF [14, 15], it was important to assess myocardial collateral blood flow and exclude the dogs with high myocardial collateral blood flow. We excluded two dogs with excessive collateral blood flow (>15 ml/100 g/min) (Control group: 1, WTMN group: 1) among 29 dogs tested. Thus, 27 dogs were

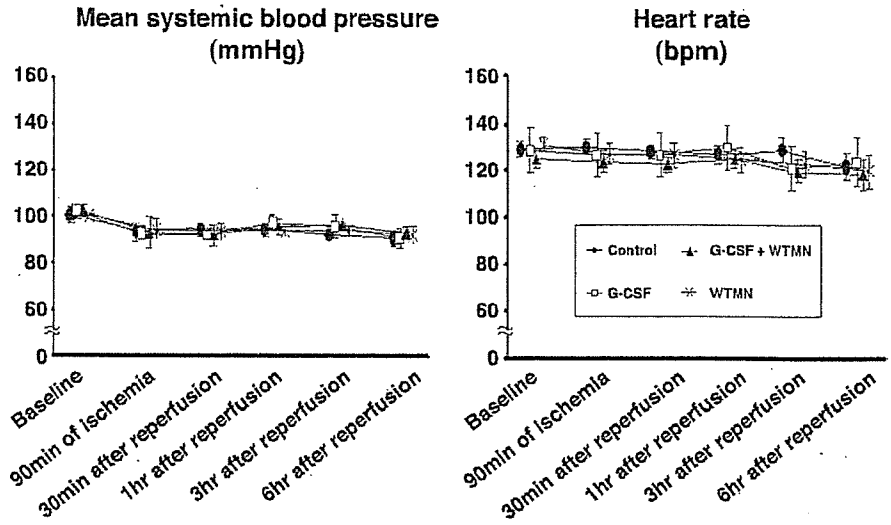

Fig. 2 The changes in mean systemic blood pressure (SBP) and heart rate (HR) during the experiment in groups tested. Neither SBP nor HR differed between the groups tested at baseline, 90 min of ischemia, at 30 min and 1, 3, and 6 h after reperfusion.

evaluated for VF analysis. Among these 27 dogs, we further excluded two dogs (Control group: 1, G-CSF + WTMN group: 1) from infarct size analysis that matched the exclusion criteria of lethal arrhythmia (more than two consecutive attempts required to convert VF with low-energy DC pulses applied directly to the heart) [10].

Effects of G-CSF on infarct size and VF during the reperfusion period

Throughout the study, neither SBP nor HR differed among the four groups (Fig. 2). The area at risk and myocardial collateral blood flow during myocardial ischemia were also comparable in the groups tested (Fig. 3). Figure 4 shows infarct size in the groups tested. G-CSF reduced ($p < 0.05$) infarct size compared with the control group. The intracoronary administration of wortmannin for 60 min after the onset of reperfusion abrogated the infarct size-limiting effects of G-CSF, although wortmannin alone did not affect infarct size.

G-CSF reduced ($p < 0.05$) the incidence of VF during the reperfusion period compared with the control group (Table 1). The antiarrhythmic effects of G-CSF were abolished by wortmannin.

Effect of G-CSF on MPO activity in infarcted myocardium

MPO activity in infarcted myocardium 6 h after reperfusion in G-CSF group did not differ from that in the control group. (10.0 ± 2.6 versus 10.7 ± 2.1 U/g protein).

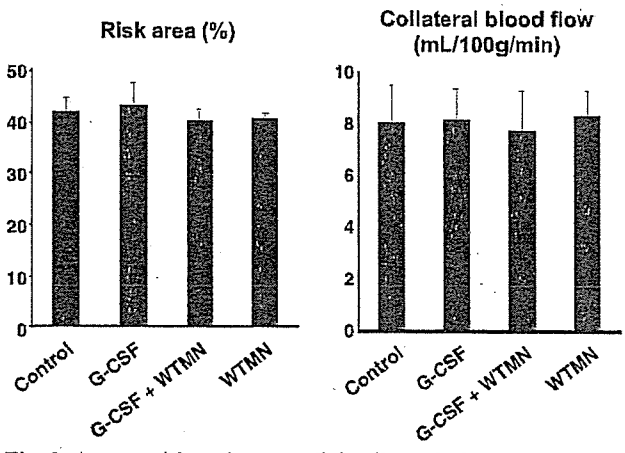

Fig. 3 Area at risk and myocardial collateral blood flow during ischemia in groups tested. Neither the area at risk nor myocardial collateral blood flow differed between the groups tested.

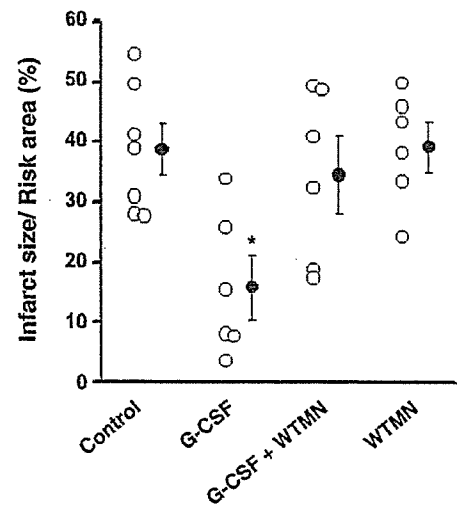

Fig. 4 Infarct size as a percentage of the area at risk in groups tested. Intravenous administration of G-CSF limited infarct size. The infarct-size limiting effect of G-CSF was blunted by the intracoronary administration of WTMN during reperfusion. *$p <$ 0.05 vs. control group.

Table 1 Effects of G-CSF on the incidence of VF during reperfusion periods

Group	Incidence of VF (%)	
Control	50.0	(4/8)
G-CSF	0*	(0/6)
G-CSF + WTMN	42.9	(3/7)
WTMN	50.0	(3/6)

*$p < 0.05$ vs. control group

Effect of G-CSF on Akt phosphorylation in ischemic myocardium

G-CSF augmented Akt phosphrylation in the LAD-perfused myocardium. The increase in Akt phosphorylation was attenuated by wortmannin (Fig. 5).

Discussion

The present study demonstrated that administration of G-CSF following the onset of reperfusion limited infarct size in acute phase and reduced the incidence of lethal arrhythmia. The intracoronary administration of wortmannin abrogated these cardioprotective effects of G-CSF, suggesting that G-CSF mediated cardioprotection via the PI3K/Akt pathway. To our knowledge, this is the first study to reveal the acute effect of G-CSF against ischemia/reperfusion injury via the PI3K/Akt pathway in in vivo canine hearts.

Previous studies have reported that G-CSF improves cardiac remodeling after MI in the chronic ligation model of coronary artery [4, 5, 16]. It has been believed that G-CSF exerts cardioprotective effects through regeneration of myocardium and angiogenesis. Recently, Komuro and colleagues clearly demonstrated that the high dose of G-CSF limits infarct size in the acute phase in the isolated hearts [6]. To translate their remarkable findings into the clinical setting, we need to consider the dose of G-CSF and experimental models in their study. They used a perfusate containing 300 ng/ml G-CSF in the isolated heart model. This dose is relatively high compared with the dose used in clinical settings [17, 18]. In addition, effects of G-CSF on neutrophil function cannot be tested in the isolated heart model. In the present study, we demonstrated that a clinical relevant dose of G-CSF acutely limits infarct size in the in vivo model. In contrast with previous studies [4, 5, 16], we examined the effects of G-CSF in the ischemia/reperfusion model, because coronary revascularization is principally applied for patients with acute MI to attenuate ischemia/reperfusion injury. We found that G-CSF following the onset of reperfusion effectively limited infarct size. Our findings strongly support that G-CSF would be a promising candidate as an adjunctive therapy for patients with acute MI. Indeed, two recent publications by the FIRSTLINE-AMI trial clearly demonstrated that subcutaneous administration of G-CSF after percutaneous coronary intervention improved cardiac function and prevented cardiac remodeling [19, 20]. Considering our present data, the improvement of cardiac function by G-CSF in clinical studies will be due to limiting infarct size in the acute phase as well as preventing cardiac remodeling.

G-CSF can provoke multiple intracellular signal transductions including Jak/Stat, ERK and PI3K/Akt [16, 21]. Recently, we and others demonstrated that post-interventions which activate PI3K/Akt during the reperfusion protect against ischemia/reprfusion injury [10, 22]. Thus, we investigated a role of PI3K/Akt in G-CSF-mediated cardioprotection. WTMN significantly blunted the infarct size-limiting effects of G-CSF, and G-CSF enhanced Akt phosphorylation in the ischemic myocardium, indicating that G-CSF reduces infarct size via PI3K/Akt-dependent pathway. Further investigations will be needed to clarify the molecular target of PI3K/Akt and the role of other signals activated by G-CSF in this condition.

Although we demonstrated that G-CSF mediated cardioprotection, one small clinical study showed that G-CSF may induce coronary re-stenosis [23]. In contrast, other large-scale studies did not show that G-CSF induced coronary restenosis [19, 20]. Since there is still controversy about the restenosis effects of G-

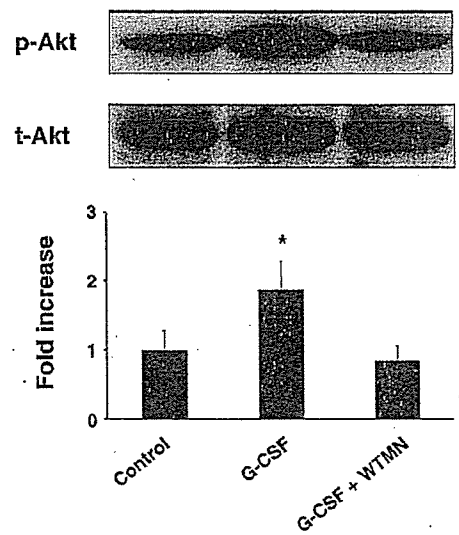

Fig. 5 Akt phosphorylation in LAD-perfused areas. G-CSF phosphorylated Akt in LAD-perfused myocardium. Akt phosphorylation by G-CSF was prevented by co-treatment with WTMN. Akt phosphorylation was normalized by total Akt. *$p < 0.05$ vs. control group.

CSF, this issue will be minimized by the concomitant use of a drug-eluting stent and G-CSF. Another possible adverse effect of G-CSF will be enhancement of neutrophil function. G-CSF appears not only to stimulate the formation of granulocyte colonies from bone marrow-derived precursors, but also to enhance the function of mature neutrophils [24] and elevates the number of white blood cells, which may predict adverse prognosis in the patients of acute MI [25]. Consistent with previous studies [26, 27], we also showed that G-CSF did not change MPO activity, a marker of neutrophil accumulation, in the infarcted myocardium. These findings suggest that G-CSF exerted cardioprotective effects independent of white blood cells. Although our findings suggest that the overall effect of G-CSF may be beneficial for ischemia/reperfused myocardium, we need to be cautious about these potential adverse effects of G-CSF.

Importantly, we clearly demonstrated that G-CSF reduced the incidence of VF during reperfusion via the PI3/Akt-dependent pathway. Since lethal arrhythmias are one of the major causes of death in patients with acute MI [8], the anti-arrhythmic effects of G-CSF have great clinical impact. We have previously demonstrated that another cytokine, erythropoietin, also reduced the incidence of lethal arrhythmia via the PI3/Akt pathway [10]. Although our findings suggest that the PI3K/Akt-dependent pathway will play an important role in the generation of lethal arrhythmias, further investigation will be needed to clarify the potential mechanism by which G-CSF exerts anti-arrhythmic effects. We need to consider whether G-CSF exerts anti-arrhythmic effects by the reduction of myocardial infarct size or by some other actions of G-CSF.

In conclusion, the intravenous administration of a clinically relevant dose of G-CSF will be a promising strategy to treat patients with acute MI. Further controlled studies will be warranted to check the safety and efficacy of G-CSF treatment in the acute phase after MI.

Acknowledgments We thank Yuko Okuda, and Yoko Nagamachi for their technical assistance.

References

1. Clark SC, Kamen R. The human hematopoietic colony-stimulating factors. Science 1987;236:1229–37.
2. To LB, Haylock DN, Simmons PJ, Juttner CA. The biology and clinical uses of blood stem cells. Blood 1997;89:2233–58.
3. Kronenwett R, Martin S, Haas R. The role of cytokines and adhesion molecules for mobilization of peripheral blood stem cells. Stem Cells 2000;18:320–30.
4. Orlic D, Kajstura J, Chimenti S, et al. Mobilized bone marrow cells repair the infarcted heart, improving function and survival. Proc Natl Acad Sci USA 2001;98:10344–9.
5. Ohtsuka M, Takano H, Zou Y, et al. Cytokine therapy prevents left ventricular remodeling and dysfunction after myocardial infarction through neovascularization. Faseb J 2004;18:851–3.
6. Harada M, Qin Y, Takano H, et al. G-CSF prevents cardiac remodeling after myocardial infarction by activating the Jak-Stat pathway in cardiomyocytes. Nat Med 2005;11:305–11.
7. Nicod P, Gilpin E, Dittrich H, et al. Late clinical outcome in patients with early ventricular fibrillation after myocardial infarction. J Am Coll Cardiol 1988;11:464–70.
8. Rouleau JL, Talajic M, Sussex B, et al. Myocardial infarction patients in the 1990s—their risk factors, stratification and survival in Canada: the Canadian Assessment of Myocardial Infarction (CAMI) Study. J Am Coll Cardiol 1996;27:1119–27.
9. Lothrop CD Jr, Warren DJ, Souza LM, Jones JB, Moore MA. Correction of canine cyclic hematopoiesis with recombinant human granulocyte colony-stimulating factor. Blood 1988;72:1324–8.
10. Hirata A, Minamino T, Asanuma H, et al. Erythropoietin just before reperfusion reduces both lethal arrhythmias and infarct size via the phosphatidylinositol-3 kinase-dependent pathway in canine hearts. Cardiovasc Drugs Ther 2005;19:33–40.
11. Maruyama R, Takemura G, Aoyama T, et al. Dynamic process of apoptosis in adult rat cardiomyocytes analyzed using 48-hour videomicroscopy and electron microscopy: beating and rate are associated with the apoptotic process. Am J Pathol 2001;159:683–91.
12. Asanuma H, Kitakaze M, Funaya H, et al. Nifedipine limits infarct size via NO-dependent mechanisms in dogs. Basic Res Cardiol 2001;96:497–505.
13. Holm S. A simple sequentially rejective multiple test procedure. Scand J Statist 1979;6:65–70.
14. Hale SL, Lange R, Alker KJ, Kloner RA. Correlates of reperfusion ventricular fibrillation in dogs. Am J Cardiol 1984;53:1397–400.
15. Bolli R, Patel B. Factors that determine the occurrence of reperfusion arrhythmias. Am Heart J 1988;115:20–9.
16. Iwanaga K, Takano H, Ohtsuka M, et al. Effects of G-CSF on cardiac remodeling after acute myocardial infarction in swine. Biochem Biophys Res Commun 2004;325:1353–9.
17. Gabrilove JL, Jakubowski A, Fain K, et al. Phase I study of granulocyte colony-stimulating factor in patients with transitional cell carcinoma of the urothelium. J Clin Invest 1988; 82:1454–61.
18. Bensinger WI, Clift RA, Anasetti C, et al. Transplantation of allogeneic peripheral blood stem cells mobilized by recombinant human granulocyte colony stimulating factor. Stem Cells 1996;14:90–105.
19. Ince H, Petzsch M, Kleine HD, et al. Prevention of left ventricular remodeling with granulocyte colony-stimulating factor after acute myocardial infarction: final 1-year results of the Front-Integrated Revascularization and Stem Cell Liberation in Evolving Acute Myocardial Infarction by Granulocyte Colony-Stimulating Factor (FIRSTLINE-AMI) Trial. Circulation 2005;112:I73–80.
20. Ince H, Petzsch M, Kleine HD, et al. Preservation from left ventricular remodeling by front-integrated revascularization and stem cell liberation in evolving acute myocardial infarction by use of granulocyte-colony-stimulating factor (FIRSTLINE-AMI). Circulation 2005;112:3097–106.
21. Avalos BR. Molecular analysis of the granulocyte colony-stimulating factor receptor. Blood 1996;88:761–77.

22. Tsang A, Hausenloy DJ, Mocanu MM, Yellon DM. Post-conditioning: a form of "modified reperfusion" protects the myocardium by activating the phosphatidylinositol 3-kinase-Akt pathway. Circ Res 2004;95:230–2.
23. Kang HJ, Kim HS, Zhang SY, et al. Effects of intracoronary infusion of peripheral blood stem-cells mobilised with granulocyte-colony stimulating factor on left ventricular systolic function and restenosis after coronary stenting in myocardial infarction: the MAGIC cell randomised clinical trial. Lancet 2004;363:751–6.
24. Weisbart RH, Golde DW, Clark SC, Wong GG, Gasson JC. Human granulocyte-macrophage colony-stimulating factor is a neutrophil activator. Nature 1985;314:361–3.
25. Barron HV, Cannon CP, Murphy SA, Braunwald E, Gibson CM. Association between white blood cell count, epicardial blood flow, myocardial perfusion, and clinical outcomes in the setting of acute myocardial infarction: a thrombolysis in myocardial infarction 10 substudy. Circulation 2000;102: 2329–34.
26. Adachi Y, Imagawa J, Suzuki Y, et al. G-CSF treatment increases side population cell infiltration after myocardial infarction in mice. J Mol Cell Cardiol 2004;36: 707–10.
27. Sugano Y, Anzai T, Yoshikawa T, et al. Granulocyte colony-stimulating factor attenuates early ventricular expansion after experimental myocardial infarction. Cardiovasc Res 2005;65:446–56.

The EMBO Journal (2006) 25, 2388–2396 | © 2006 European Molecular Biology Organization | All Rights Reserved 0261-4189/06
www.embojournal.org

THE EMBO JOURNAL

Crystal structures of VAP1 reveal ADAMs' MDC domain architecture and its unique C-shaped scaffold

Soichi Takeda[1,2,*], Tomoko Igarashi[1], Hidezo Mori[1] and Satohiko Araki[3]

[1]Department of Cardiac Physiology, National Cardiovascular Center Research Institute, Suita, Osaka, Japan, [2]Laboratory for Structural Biochemistry, Riken Harima Institute at SPring-8, Mikazuki, Sayo, Hyogo, Japan and [3]Sugashima Marine Biological Laboratory, Graduate School of Science, Nagoya University, Toba, Mie, Japan

ADAMs (a disintegrin and metalloproteinase) are sheddases possessing extracellular metalloproteinase/disintegrin/cysteine-rich (MDC) domains. ADAMs uniquely display both proteolytic and adhesive activities on the cell surface, however, most of their physiological targets and adhesion mechanisms remain unclear. Here for the first time, we reveal the ADAMs' MDC architecture and a potential target-binding site by solving crystal structures of VAP1, a snake venom homolog of mammalian ADAMs. The D-domain protrudes from the M-domain opposing the catalytic site and constituting a C-shaped arm with cores of Ca^{2+} ions. The disintegrin-loop, supposed to interact with integrins, is packed by the C-domain and inaccessible for protein binding. Instead, the hyper-variable region (HVR) in the C-domain, which has a novel fold stabilized by the strictly conserved disulfide bridges, constitutes a potential protein–protein adhesive interface. The HVR is located at the distal end of the arm and faces toward the catalytic site. The C-shaped structure implies interplay between the ADAMs' proteolytic and adhesive domains and suggests a molecular mechanism for ADAMs' target recognition for shedding.

The EMBO Journal (2006) 25, 2388–2396. doi:10.1038/sj.emboj.7601131; Published online 11 May 2006
Subject Categories: signal transduction; structural biology
Keywords: ADAM; MDC; protein–protein interaction shedding; snake venom metalloproteinase

Introduction

ADAMs (a disintegrin and metalloproteinase) or MDC (metalloproteinase/disintegrin/cysteine-rich) proteins comprise an emerging class of mammalian metalloproteinases with potential regulatory roles in cell–cell and cell–matrix adhesion and signalling (Becherer and Blobel, 2003; Seals and Courtneidge, 2003; White, 2003; Blobel, 2005). To date, over 30 ADAMs have been identified in a variety of species from fission yeast to human. Roughly, half of these are believed to function as active metalloproteinases and thus to constitute major membrane-bound sheddase that can proteolytically release cell-surface-protein ectodomains including growth factors and cytokines, their receptors and cell adhesion molecules. For example, ADAM17 (TACE, TNF-α converting enzyme) releases many cell-surface proteins including TNF-α precursor (Black *et al*, 1997; Moss *et al*, 1997) and ADAM10 (kuzbanian), which dictates lateral inhibition of *Drosophila* neurogenesis (Rooke *et al*, 1996), releases Notch ligand Delta (Qi *et al*, 1999) and Notch itself (Pan and Rubin, 1997). With regard to cellular interactions, fertilin α and β (ADAM1 and ADAM2, respectively) have been identified as sperm surface molecules essential for fertilization (Primakoff *et al*, 1987; Blobel *et al*, 1990, 1992) and meltrin α (ADAM12) is implicated in myogenesis (Yagami-Hiromasa *et al*, 1995). ADAMs have been associated with numerous diseases including arthritis, Alzheimer's disease, and cancer (Duffy *et al*, 2003; Moss and Bartsch, 2004). ADAM33 has been genetically linked with asthma (Van Eerdewegh *et al*, 2002). ADAMs uniquely display both proteolytic and adhesive activities on the cell surface, however, most of their physiological targets and the adhesion mechanisms remain unclear.

Disintegrins are small proteins (40–90 aa) isolated from snake venom typically with an Arg-Gly-Asp (RGD) recognition sequence on an extended loop (disintegrin-loop) that inhibit platelet aggregation via integrin binding (Huang *et al*, 1987; Calvete *et al*, 2005). ADAMs are unique among cell surface proteins in possessing a disintegrin (D-) domain and thus it has been suggested that integrins might be common receptors for ADAMs (Blobel *et al*, 1992; Evans, 2001; White, 2003). However, the RGD sequence in the ADAMs' disintegrin-loop is usually replaced by XXCD and therefore, its adhesive potential has been controversial. Both the ADAMs' D- and cysteine-rich (C-) domains are involved in the protein–protein interactions (Myles *et al*, 1994; Almeida *et al*, 1995; Zolkiewska, 1999; Iba *et al*, 2000; Gaultier *et al*, 2002; Smith *et al*, 2002), however, the details of the interactions have remained elusive. This is because high-resolution structures have been available only for isolated domains (Maskos *et al*, 1998; Orth *et al*, 2004; Janes *et al*, 2005) and no structural information has been available for the C-domain of the canonical ADAMs. To clarify the molecular mechanisms of target recognition for shedding by and of cellular adhesion via ADAMs, elucidation of the atomic structure of the ADAMs' MDC domains is indispensable.

To obtain structural data on an ADAM family member, we exploited the fact that hemorrhagic P-III snake venom metalloproteinases (SVMPs) share the ADAMs' MDC architecture (Jia *et al*, 1996; Evans, 2001; Fox and Serrano, 2005). Most ADAMs possess additionally, EGF-like, transmembrane and cytoplasmic domains and therefore are primarily membrane-associated, whereas SVMPs are secreted. Vascular apoptosis-inducing protein-1 (VAP1) is a disulfide-bridged

*Corresponding author. Department of Cardiac Physiology, National Cardiovascular Center Research Institute, Fujishirodai 5-7-1, Suita, Osaka, 565-8565, Japan. Tel.: +81 6 6833 5012 ext.2381; Fax: +81 6 6872 7485; E-mail: stakeda@ri.ncvc.go.jp

Received: 17 February 2006; accepted: 12 April 2006; published online: 11 May 2006

homodimer P-III SVMP isolated from *Crotalus atrox* venom (Masuda *et al*, 1998, 2000). VAP1's stability and intrinsic two-fold symmetry enabled us to solve the crystal structures at 2.5-Å resolution. The structure reveals the residues that are important for stabilizing the MDC architecture are strictly conserved throughout the primary structure among all the known ADAMs. Therefore, the present structure represents the general architecture of ADAMs' MDC domains and provides insights into the molecular mechanism of the ADAMs' target recognition.

Results

Structure determination

VAP1 yielded crystals readily, and initial phases were determined by molecular replacement method using the structure of P-I SVMP, acutolysin-C (1QUA) (Zhu *et al*, 1999) as a starting model. Although the initial model, with 99 identical residues out of 197, represented less than 50% of the total molecule, two distinct local noncrystallographic two-fold symmetry (NCS) operations (see below) allowed us to completely model the whole molecule. The native structures were determined from the crystals with two distinct space groups, $P2_12_12_1$ and $P4_12_12$, both at 2.5-Å resolution (Table I). Orthorhombic crystals were used for inhibitor soaking and the GM6001 ((3-(*N*-hydroxycarboxamido)-2-isobutyl-propanoyl-Trp-methylamide))-bound structure was determined at 3.0-Å resolution (Table I). In either crystal forms, the asymmetric unit contained one dimer molecule. The four monomers in the two crystal forms have almost identical structures, except for slight variations in their domain orientations, terminal residues, surface loops and active-site GM6001-binding region.

MDC architecture

The MDC architecture of VAP1 is shown in Figure 1A and B. The metalloproteinase (M-) domains in the dimer are related by NCS such that their active sites point in opposite directions and an intermolecular disulfide bridge is formed between symmetry-related Cys365 residues (Figure 1A). The M-domain is followed by a disintegrin (D-) domain that is further divided into D_s- and D_a-domains (see below). The D_s-domain protrudes from the M-domain close to the Ca^{2+}-binding site I (see below) opposing the catalytic site. The D-domain forms a C-shaped arm, together with the cysteine-rich (C-) domain, with its concave surface toward the M-domain. There are no direct interactions between the arm and the M-domain. Notably, the distal portion of the C-domain comes close to

Table I Data collection and refinement statistics

	Native (orthorhombic)	Native (tetragonal)	GM6001-bound
Data collection			
Space group	$P2_12_12_1$	$P4_12_12$	$P2_12_12_1$
Cell dimensions			
a, *b*, *c* (Å)	86.7, 93.3, 137.7	93.9,93.9,244.8	86.3, 91.4, 136.0
α, β, γ (deg)	90, 90, 90	90, 90, 90	90, 90, 90
Resolution (Å)	50–2.50 (2.59–2.50)	50–2.50 (2.59–2.50)	50–2.95 (3.06–2.95)
R_{merge}[a]	0.072 (0.369)	0.084 (0.380)	0.072 (0.367)
$I/\sigma I$	14.4 (2.9)	18.7 (7.1)	12.6 (4.3)
Completeness (%)	99.4 (98.8)	99.7 (99.6)	99.9 (99.4)
Redundancy	3.91	12.7	4.95
Refinement			
Resolution (Å)	50–2.50 (2.59–2.50)	50–2.50 (2.59–2.50)	50–2.95 (3.06–2.95)
No. of reflections	38874	38786	23295
R_{work}[b]/R_{free}[c]	0.212/0.258	0.229/0.269	0.208/0.264
No. of atoms			
Protein	6558	6513	6558
Zn^{2+}	2	2	2
Ca^{2+}	4	4	4
Co^{3+}	1		1
N-acetyl glucosamine	56	42	56
GM6001			56
Water	205	165	35
B-factors			
Protein	44.9	51.2	55.4
Zn^{2+}	40.9	41.6	46.4
Ca^{2+}	43.5	52.4	49.3
Co^{3+}	35.5		56.8
N-acetyl glucosamine	69.8	65.1	75.8
GM6001			78.6
Water	39.8	41.5	37.0
R.m.s deviations			
Bond lengths (Å)	0.0052	0.0080	0.0038
Bond angles (deg)	1.18	1.39	0.92

[a] $R_{merge} = \sum_{hkl}\sum_i |I_i(hkl) - \langle I(hlk)\rangle| \;/\; \sum_{hkl}\sum_i I_i(hkl)$, where $I_i(hkl)$ is the *i*th intensity measurement of reflection *hkl* and $\langle I(hlk)\rangle$ is its average.

[b] $R_{work} = \sum(||F_{obs}| - |F_{calc}||)/\sum|F_{obs}|$.

[c] R_{free} = *R*-value for a randomly selected subset (5%) of the data that were not used for minimization of the crystallographic residual.

Highest resolution shell is shown in parenthesis.

For each data set, single crystal was used for measurement.

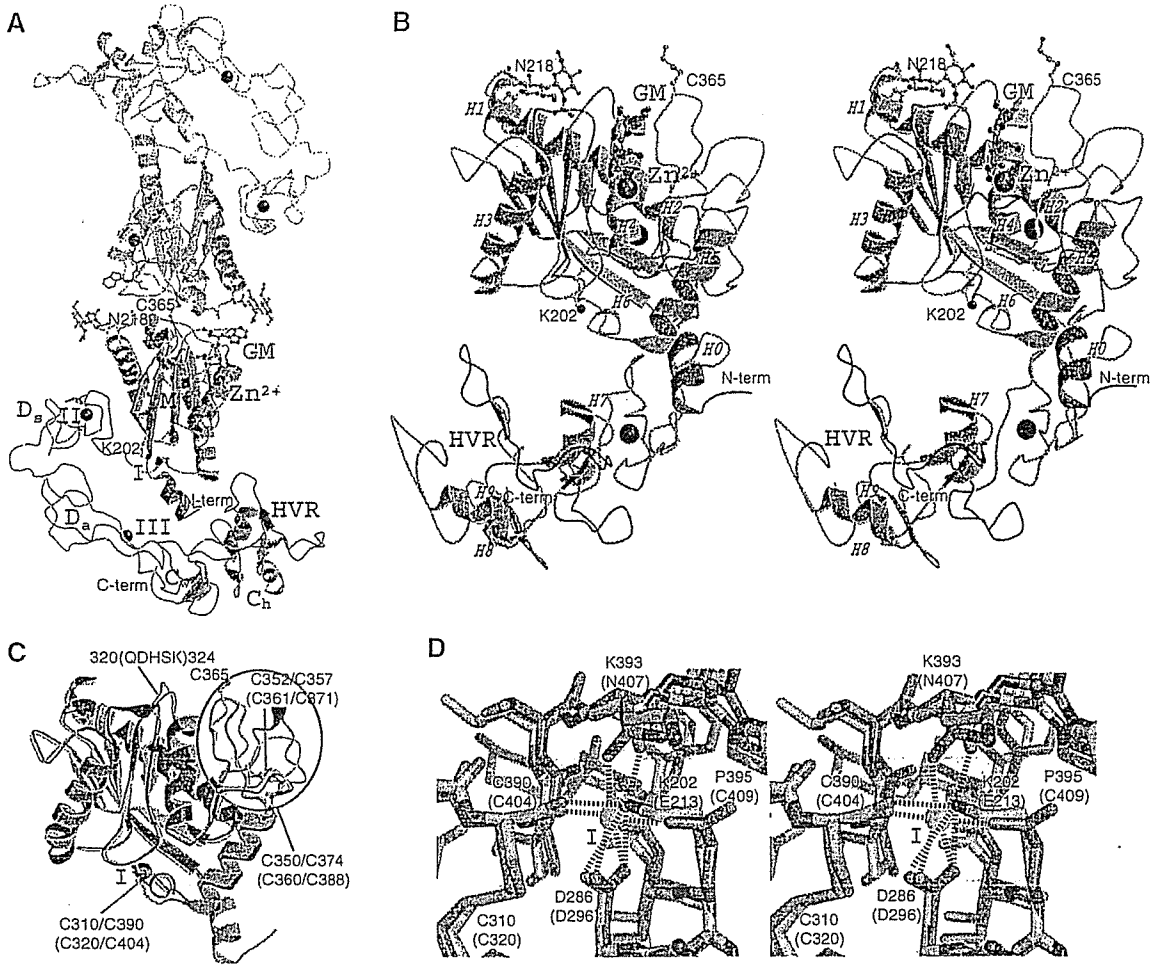

Figure 1 MDC architecture. (A) VAP1 dimer viewed from the NCS axis. The H0-helix, M-domain, linker, D_s-, D_a-, C_w-, and C_h-domains and HVRs belonging to the one monomer are shown in red, yellow, gray, cyan, pink, gray, green and blue, respectively. The disulfide-linked counterpart is shown in gray. Zinc and calcium ions are represented as red and black spheres, respectively. The NAG (*N*-acetyl-glucosamine, in orange) moieties linked to Asn218, the calcium-mimetic Lys202 and the bound inhibitor GM6001 (GM, in green) are in ball-stick representations. (B) Stereo view of VAP1 monomer from the direction nearly perpendicular to (A). The helix numbers are labelled. (C) Superposition of the M-domains of ADAM33 (blue) and VAP1 (yellow). The calcium ion bound to site I and the zinc ion in ADAM33 are represented by black and red spheres, respectively. The disulfide bridges are indicated in black and blue letters for VAP1 and ADAM33, respectively. The QDHSK sequence for the dimer interface in VAP1 (residues 320–324) is in red. (D) Comparison of the calcium-binding site I structures of ADAM33 (blue) and VAP1 (yellow) *in stereo*. The residues in ADAM33 and in VAP1 are labelled in blue and black, respectively. A calcium ion and a water molecule bound to ADAM33 are represented as green and red spheres, respectively. The ammonium group of Lys202 in VAP1 occupies the position of the calcium ion in ADAM33. In ADAM33 (Orth *et al*, 2004), side-chain oxygen atoms of Glu213, Asp296 and Asn407, the carbonyl oxygen of Cys404 and a water molecule form the corners of a pentagonal bipyramid and ligand to the calcium ion.

and faces toward the catalytic site in the M-domain. The C-terminus Tyr610 is located proximal to the boundary between the D_a- and C-domains (Figure 1A and B). Aside from Cys365, each monomer contains 34 cysteinyl residues, all of which are involved in disulfide bonding, and their spacings are strictly conserved among ADAMs (Figure 2 and Supplementary Figure 1) except within the substrate-binding (between the helices H4 and H5) and the HVR (see below) regions. Figure 2 provides a selected subset of the sequence alignments and the entire alignments of VAP1 and 39 ADAM sequences, including all 23 human ADAMs so far available, can be found as Supplementary Figure 1.

M-domain

Each VAP1 M-domain corresponds to a very similar structure to that of ADAM33 (Orth *et al*, 2004), with a flat ellipsoidal shape having a central core made up of five stranded β-sheets and five α-helices and a conserved methionine (Met-turn) below the active site histidine residues, which bears the typical structural feature of metzincin family of metalloproteinases (Bode *et al*, 1993). However, they differ in the dimer interface and the loop structure around the substrate-binding site (Figure 1C) that corresponds to the variable region in the primary structure (between the helices H4 and H5, see Figure 2). The N-terminal helix (H0) is also unique in VAP1. The dimer interface is best characterized by the recognition sequence QDHSK (residues 320–324, see Figure 1C and Supplementary Figure 2A–C) and by Cys365, however these are not conserved among ADAMs; therefore, none of the ADAMs' M-domains are suggested to form a stable dimer as VAP1. A peptide-like hydroxamate inhibitor GM6001 binds to VAP1 (Figure 1A and B, and Supplementary Figure 2D and E) in exactly the same manner as in the marimastat-ADAM33 M-domain complex (Orth *et al*, 2004), suggesting that the catalytic sites of VAP1 and ADAM33 share a common substrate recognition mechanism. The ADAM33

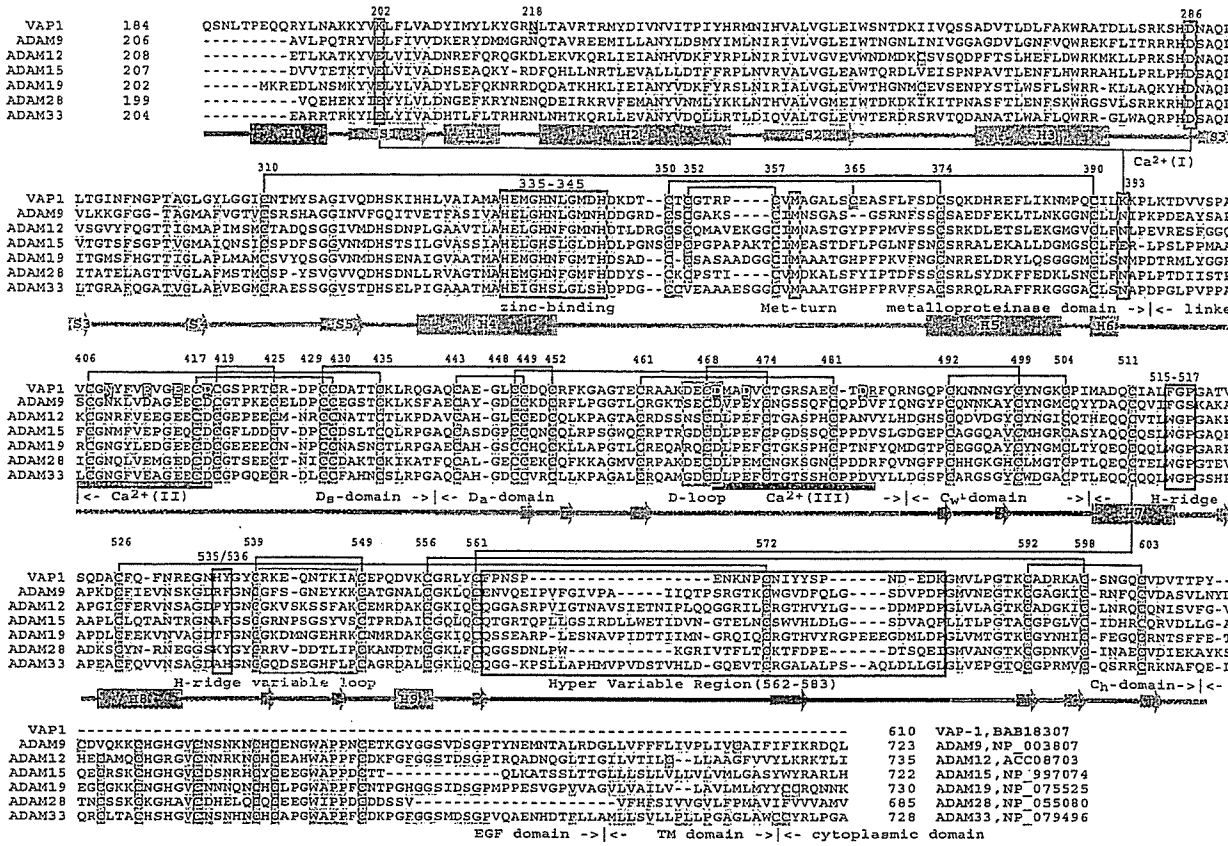

Figure 2 Sequence alignments of VAP1 and human ADAMs. The cysteinyl residues and the conserved residues are shaded in pink and yellow, respectively. Disulfide bridges, secondary structures and domains are drawn schematically. The HVR, calcium-binding site I, catalytic site and disintegrin-loop (D-loop) are boxed in blue, red, green and cyan, respectively. The hydrophobic ridges (H-ridges) are indicated. Calcium-binding sites II and III and the coordinating residues (shaded in red) are indicated. The NCBI accession numbers for the sequences are indicated.

M-domain structure suggests that most ADAMs have a Ca^{2+}-binding site (designated Ca^{2+}-binding site I) opposing the active-site cleft; however, in VAP1, the distal ammonium group of Lys202 substitutes for the Ca^{2+} ion (Figure 1D). Replacement of the calcium-coordinating glutamate residue with lysine also occurs in ADAM16, ADAM25 and ADAMs38–40 (Supplementary Figure 1).

C-shaped arm

The D-domain follows the M-domain, with a short linker that allows slightly variable domain orientations at V405 as a pivotal point (Figure 3C). The D-domain is further divided into two structural subdomains (Figure 3), the 'shoulder' (D_s-domain, residues 396–440) and the 'arm' (D_a-domain, residues 441–487). The D_s- and D_a-domains constitute a continuous C-shaped arm, together with the following N-terminus region of the C-domain which we designate the 'wrist' (C_w-domain, residues 488–505). There are three disulfide bonds in the D_s-domain, three in the D_a-domain and one in the C_w-domain. The subdomains are connected by single disulfide bridges (Figures 2 and 3A) with slightly variable angles (Figure 3B).

Both the D_s- and D_a-domains contain structural calcium-binding sites. In the D_s-domain, the side-chain oxygen atoms in residues Asn408, Glu412, Glu415 and Asp418, and the carbonyl oxygen atoms of Val405 and Phe410 are involved in pentagonal bipyramidal coordination and constitute Ca^{2+}-binding site II (Figures 2 and 3A). Notably, these residues are strictly conserved among all known ADAMs (Supplementary Figure 1). However, the side-chain oxygens of Asp469, Asp472 and Asp483, and carbonyl oxygens of Met470 and Arg484 form the corners of a pentagonal bipyramid to the calcium ligand and constitute the D_a-domain Ca^{2+}-binding site III (Figures 2 and 3A) and these residues are highly conserved among ADAMs except ADAM10 and ADAM17 (Supplementary Figure 1). Because of the few secondary-structural elements, bound calcium ions and the disulfide bridges are essential for the structural rigidity of ADAM's C-shaped arm. The RGD-containing disintegrin trimestatin (Fujii *et al*, 2003) has a similar structure with the D_a-domain (r.m.s.d of 1.24 Å, Figure 3B); however, no disintegrins have been shown to bind Ca^{2+} ions.

Using isolated D-domains or portions thereof, numerous ADAMs and P-III SVMPs have been shown to interact specifically with particular integrins (Evans, 2001; White, 2003; Calvete *et al*, 2005). However, the disintegrin-loop is packed against the C_w-domain and a disulfide bridge (Cys468–Cys499) further stabilizes the continuous structure (Figure 3A). Therefore, the disintegrin-loop is inaccessible for protein binding.

Hand domain

The 'hand' domain (C_h-domain, residues 505–610) follows the C_w-domain. The C_h-domain, together with the C_w-domain, constitutes a novel fold (Figure 4A). In either crystal form, VAP1 dimers interact with molecules of neighboring

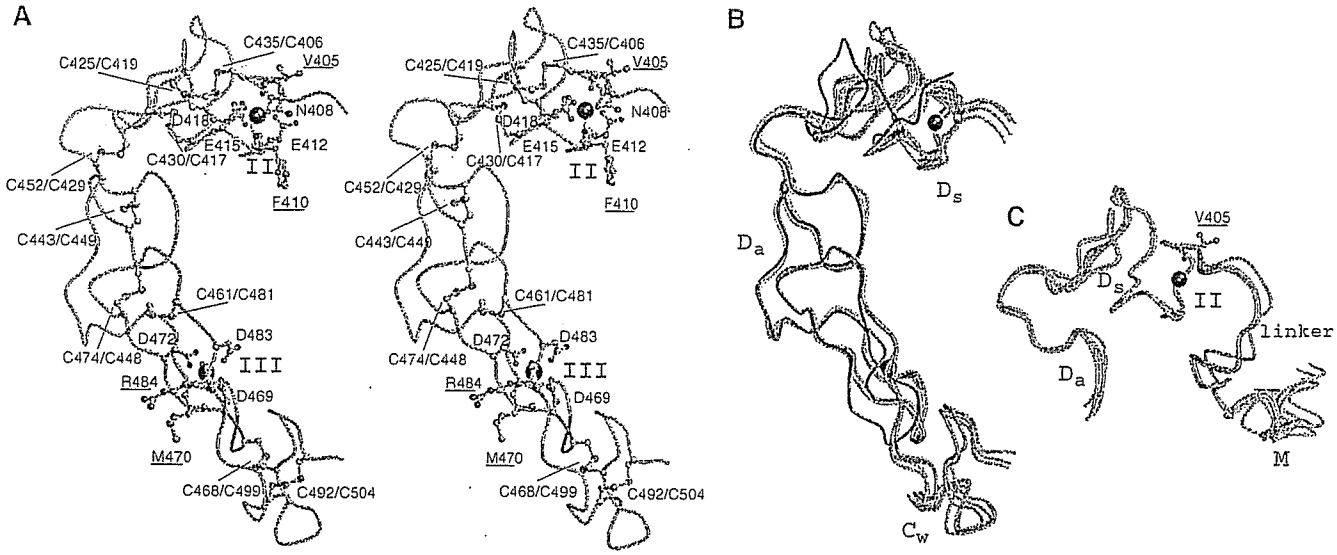

Figure 3 Arm structure. (A) Arm structure *in stereo*. The D_s-, D_a-, and C_w-domains are in cyan, pink and light green, respectively. The calcium-coordinating residues and the disulfide bridges are shown in red and green, respectively. The residues with carbonyl oxygen atoms involved in calcium coordination are underlined. Calcium ions are represented as black spheres. The disintegrin-loop (DECD) is in blue. (B) Superimposition of the four D_a-domains of VAP1 and trimestatin (1J2L). Trimestatin and its RGD loop are shown in red and blue, respectively. (C) Superimposition of the four D_s-domains. The linker between the M- and D_s-domains is shown in gray. Val405 at the pivotal point is indicated.

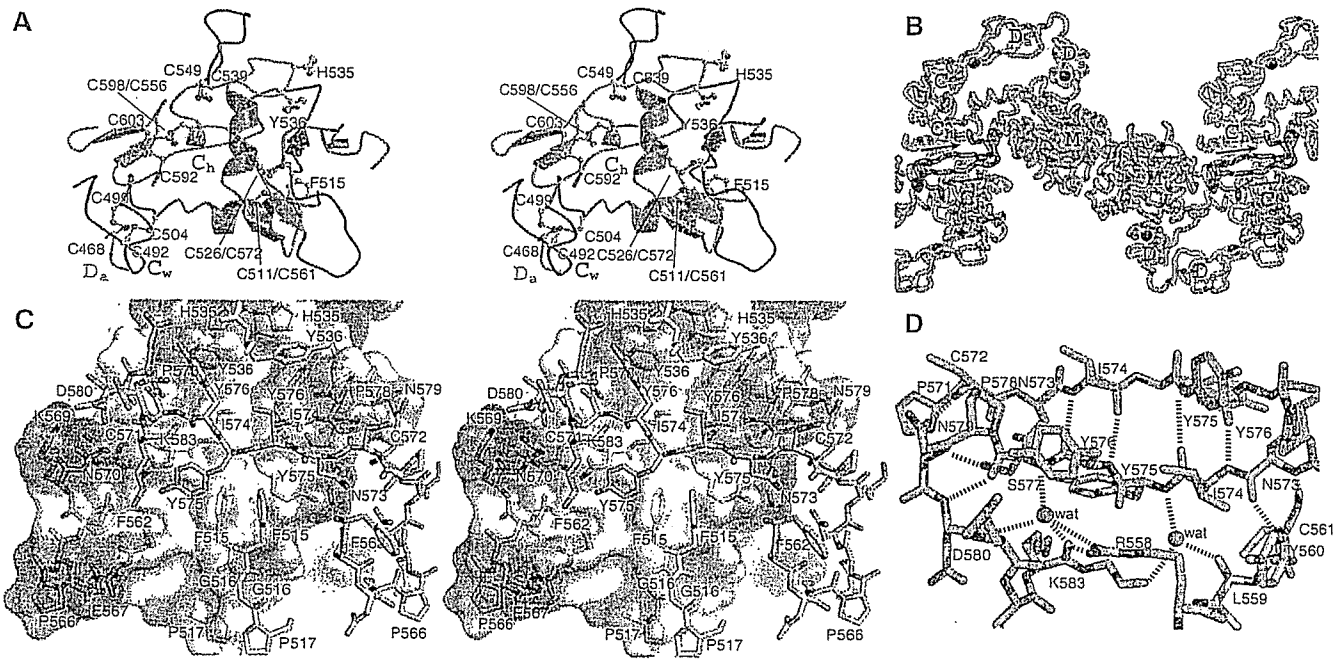

Figure 4 C-domain architecture and HVR. (A) The C-domain architecture *in stereo*. The C_w- and C_h-domains are in gray and light green, respectively. The disulfide bridges and the residues forming the hydrophobic ridges are indicated. The HVR and its NCS counterpart are shown in red and blue, respectively. The variable loop (residues 539–549), flanked by two adjacent cysteine residues, is in green. (B) Crystal packing in the orthorhombic crystal. The crystallographically equivalent molecules (HVRs) are in cyan (blue) and pink (red), respectively. The arrows indicate the directions of the HVR chains. Zinc and calcium ions are represented as red and black spheres, respectively. (C) Interactions between the HVRs (cyan and pink) *in stereo*. The molecular surface of the cyan molecule is shown with the electrochemical surface potential (red to blue). The residues constituting the hydrophobic ridges are in yellow. The residues are labelled in blue and red for cyan and pink, respectively. (D) Water-mediated hydrogen-bond network in the HVR. The HVR residues are in pink and cyan; non-HVR residues in the pink molecule are in gray.

units through the C_h-domains such that the molecules form a handshake (Figure 4B). Each C_h-domain interacts with its counterpart through a relatively large complementary surface of 860 Å^2 forming another NCS at the center, although VAP1 exists as dimers, not as oligomers, and is mono-dispersed in solution (data not shown).

HVR as a potential adhesive interface

C_h-domain residues 562–583 are predominantly involved in the handshake (Figure 4B). This is the region in which the ADAM sequences are most divergent and variable in length (16–55 aa) (Figure 2 and Supplementary Figure 1). We have designated this as the hyper-variable region (HVR). The HVR

is subdivided into two structural elements. The N-terminal portion (residues 562–572) fits into an extended loop, filling the gap between the M-domain and the neighboring molecule's C_h-domain and thus fixing the position of the arm (Figure 4B). The variable structures and less-specific interactions suggest that this loop is stabilized by crystal packing. Some ADAMs possess a putative fusion peptide in this segment typical of viral fusion proteins (Blobel *et al*, 1992; Yagami-Hiromasa *et al*, 1995), although their role in the actual fusion process has not been demonstrated. However, the remainder of the HVR (residues 572–583) interacts extensively with its counterpart by forming an antiparallel β strand at the center (Figure 4C and D). Although the ability to form β strand is predictable from the sequence, this β strand is stabilized mainly by interchain interactions (Figure 4D). There are no intrachain hydrogen bonds between residues 574–577 and the remainder of the C_h-domain; however a water-mediated hydrogen-bond network stabilizes this segment (Figure 4D). Therefore, it appears, that this β strand might be formed by the induced-fit mechanism upon the association of the C_h-domains and that the conserved disulfide bond (Cys526–Cys572, see Figure 4D) may stabilize the structure when the HVRs are isolated in solution. In addition to the main-chain hydrogen bonds, side-chain atoms (particularly residues I574, Y575, Y576 and P578) in the HVR β strand contribute numerous von der Waals interactions with their counterparts. Aside from the HVR, aromatic residues located at both sides of the β strand in close proximity to the NCS axis create additional interaction surfaces: residues Phe515, Gly516, His535 and Tyr536 in the loop regions form hydrophobic ridges that fit complementarily into the NCS region (Figure 4C). The hydrophobic ridges are highly conserved among ADAMs (Figure 2 and Supplementary Figure 1), thus, in part, they may also constitute binding surfaces.

Discussion

The VAP1 structures reveal highly conserved structural calcium-binding sites and the numbers and the spacings of cysteinyl residues that are essential for maintaining structural rigidity and spatial arrangement of the ADAMs' MDC domains. The C-shaped MDC architecture implies meaningful interplay between the domains and their potential roles in physiological functions.

The HVR creates a novel interaction interface in collaboration with the conserved hydrophobic ridges. Different ADAMs have distinct HVR sequences, which result in distinct surface features, thus, they may function in specifying binding proteins. The HVR is at the distal end of the C-shaped arm and points toward the M-domain catalytic site, with a distance of ~4 nm in between them. Collectively, these observations suggest that the HVR captures the target or associated protein that is processed by the catalytic site (Figure 5). The disintegrin portion is located opposit to and apart from the catalytic site and, thus, might play a primary role as a scaffold that allocates these two functional units spatially. The C-shaped structure also implies how the ADAMs' C-domains cooperate with their M-domains (Reddy *et al*, 2000; Smith *et al*, 2002). In membrane-bound ADAMs, the EGF-like domain (~60 aa) follows the C_h-domain (Figure 2) and presumably works as a rigid spacer connecting the MDC-domains with and orientating against the membrane-spanning region (Figure 5A). Many ADAMs are proteolytically inactive (because of the defects in the catalytic HEXXHXXGXXHD sequence or the post-translational removal of the M-domain), and several of these are important developmentally. Therefore, the HVR may also work to modulate cell–cell and cell–matrix interactions. There is some experimental evidence for C-domain-mediated adhesion. Peptides encompassing the HVR and the hydrophobic ridge from P-III SVMPs interfere with platelet interaction and collagen binding (Kamiguti *et al*, 2003). A recombinant atrolysin-A C-domain specifically binds collagen I and von Willebrand factor (vWF) and blocks collagen–vWF interaction (Jia *et al*, 2000; Serrano *et al*, 2005). ADAM12 interacts with cell-surface syndecan through its C-domain and mediates integrin-dependent cell spreading (Iba *et al*, 2000). The D/C-domain portion of ADAM13 binds to the ECM proteins laminin and fibronectin (Gaultier *et al*, 2002). However, most of these studies do not assign specific regions of the C-domain to these interactions and the molecular recognition mechanisms are to be elucidated.

ADAM10 and ADAM17 lack the Ca^{2+}-binding site III and show less sequence similarities in the C-domain with other

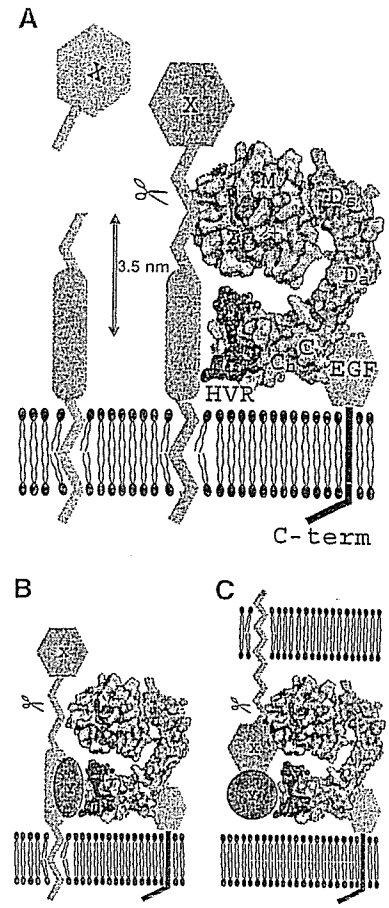

Figure 5 Models for ADAM's shedding. The molecular surface of the VAP1 monomer, without VAP1's unique H0-helix, are colored as in Figure 1A. Hydrophobic ridges are in yellow. EGF-like, transmembrane and cytoplasmic domains are represented schematically. (A) Membrane-anchored substrate molecule 'X' is directly recognized and captured by the HVR on the membrane-bound ADAM molecule. The distance between the center of the HVR (Tyr575) and the catalytic zinc ion is about 3.5 nm. (B) Substrate 'X' is recognized by the ADAM HVR via binding with an associated protein 'Y'. (C) ADAM cleaves substrate 'X' in *trans* via binding with an associated protein 'Y'.